JACS JOURNAL OF THE AMERICAN CHEMICAL SOCIETY

pubs.acs.org/JACS Article

# Giant Redox Entropy in the Intercalation vs Surface Chemistry of Nanocrystal Frameworks with Confined Pores

Jiawei Huang, Checkers R. Marshall, Kasinath Ojha, Meikun Shen, Stephen Golledge, Kentaro Kadota, Jacob McKenzie, Kevin Fabrizio, James B. Mitchell, Faiqa Khaliq, Audrey M. Davenport, Michael A. LeRoy, Ashley N. Mapile, Tekalign T. Debela, Liam P. Twight, Christopher H. Hendon, and Carl K. Brozek*

Cite This: J. Am. Chem. Soc. 2023, 145, 6257−6269 Read Online

ACCESS | Metrics & More | Article Recommendations | Supporting Information

**ABSTRACT:** Redox intercalation involves coupled ion-electron motion within host materials, finding extensive application in energy storage, electrocatalysis, sensing, and optoelectronics. Monodisperse MOF nanocrystals, compared to their bulk phases, exhibit accelerated mass transport kinetics that promote redox intercalation inside nanoconfined pores. However, nanosizing MOFs significantly increases their external surface-to-volume ratios, making the intercalation redox chemistry into MOF nanocrystals difficult to understand due to the challenge of differentiating redox sites at the exterior of MOF particles from the internal nanoconfined pores. Here, we report that Fe(1,2,3-triazolate)$_2$ possesses an intercalation-based redox process shifted ca. 1.2 V from redox at the particle surface. Such distinct chemical environments do not appear in idealized MOF crystal structures but become magnified in MOF nanoparticles. Quartz crystal microbalance and time-of-flight secondary ion mass spectrometry combined with electrochemical studies identify the existence of a distinct and highly reversible $Fe^{2+}/Fe^{3+}$ redox event occurring within the MOF interior. Systematic manipulation of experimental parameters (e.g., film thickness, electrolyte species, solvent, and reaction temperature) reveals that this feature arises from the nanoconfined (4.54 Å) pores gating the entry of charge-compensating anions. Due to the requirement for full desolvation and reorganization of electrolyte outside the MOF particle, the anion-coupled oxidation of internal $Fe^{2+}$ sites involves a giant redox entropy change (i.e., 164 J $K^{-1}$ $mol^{-1}$). Taken together, this study establishes a microscopic picture of ion-intercalation redox chemistry in nanoconfined environments and demonstrates the synthetic possibility of tuning electrode potentials by over a volt, with profound implications for energy capture and storage technologies.

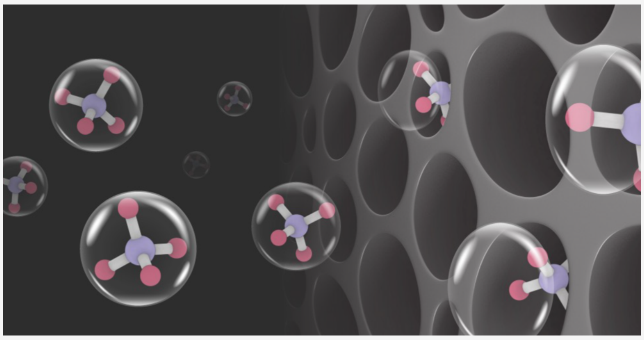

## INTRODUCTION

Metal−organic frameworks (MOFs) attract intense scientific interest in the field of electrochemical energy storage and conversion[1−9] because their tunable pore sizes and large surface areas allow facile transport of electrolytes and provide a high density of electroactive sites for driving electrochemistry.[10,11] Distinct from the electrochemical reactions of conventional nonporous electrodes, electrolyte species intercalate into the nanoconfined pores of MOFs to compensate redox events in an ion-coupled charge transport mechanism.[12−15] Previous studies of porous materials indicate that nanoconfined environments alter the identity of solvated and intercalated electrolyte species, which, in turn, dictates the resulting electrochemical performance.[16−19] For instance, reducing the pore apertures of carbon-based materials below the diameters of solvated electrolytes greatly improves the electrode capacitance by forcing closer contact between ions and the carbon surface.[16] Similar enhancement of capacitive charge storage has also been observed in two-dimensional layered birnessite, where nanoconfined intercalation environments decrease contact distances between cations and the materials.[18] In comparison, MOFs provide even greater opportunities to manipulate nanoconfined environments by altering the diverse set of available organic linkers to precise length scales and chemical compositions.[20,21] A fundamental understanding of redox chemistry within MOF pores would have direct implications for the design of wide-ranging electrochemical technologies involving intercalation redox

**Received:** December 2, 2022
**Published:** March 9, 2023

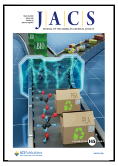

https://doi.org/10.1021/jacs.2c12846

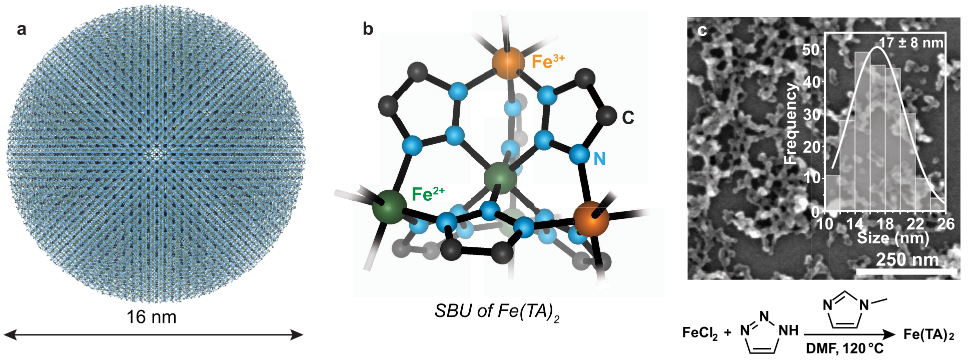

**Figure 1.** Fe(TA)$_2$ nanoparticles. (a) Idealized representation of a 16-nm Fe(TA)$_2$ nanoparticle based on the bulk crystalline structure. (b) Secondary building unit (SBU) cluster of Fe(TA)$_2$, showing the Fe$^{2+}$/Fe$^{3+}$ redox centers. (c) SEM images of 17-nm Fe(TA)$_2$ nanoparticles and the synthetic method to Fe(TA)$_2$ nanoparticles using 1-mIm as a modulator.

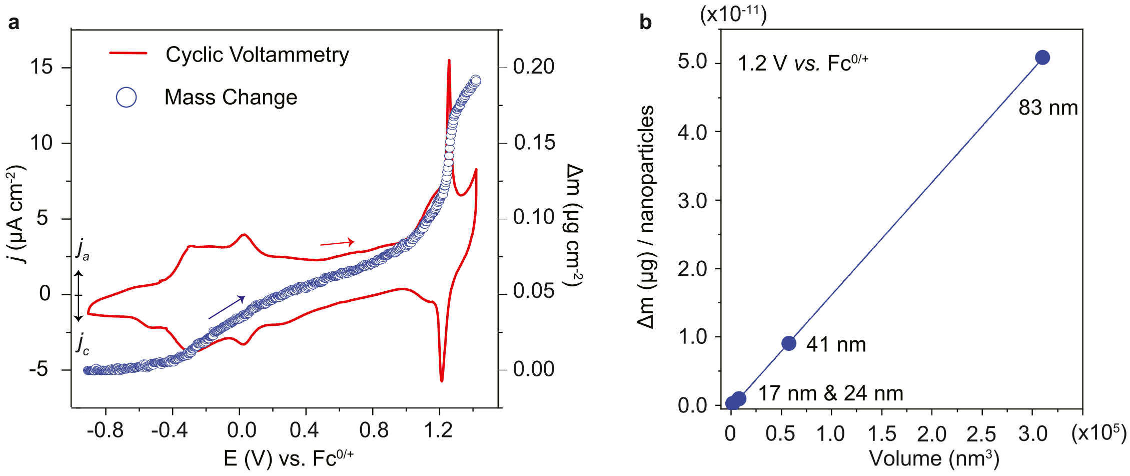

**Figure 2.** EQCM measurements of Fe(TA)$_2$ nanoparticle thin films. (a) CV (red) and mass change (blue) of Fe(TA)$_2$ nanoparticle film collected at a 10-mV/s scan rate using 0.1 M tetrabutylammonium tetrafluoroborate (TBABF$_4$) as electrolyte in acetonitrile. Scan directions are indicated by arrows and only the mass change in the anodic scan direction is shown. The spin-coating amount of 17-nm Fe(TA)$_2$ nanoparticles onto EQCM crystal is ca. 4.0 $\mu$g (i.e., ca. 21 nm in film thickness). (b) Mass change at the redox feature of 1.2 V vs Fc$^{0/+}$ as a function of nanoparticle volume for Fe(TA)$_2$ films prepared by different sizes of nanoparticles. Mass change is compared in the single-nanoparticle level due to the various loading amounts of Fe(TA)$_2$ films prepared by four different nanoparticle sizes.

events, such as batteries, bioelectronics, and capacitors. However, although recent reports have studied the impact of MOF pore sizes on the dynamics of ion intercalation (mass transport),[22] nanoconfinement effects remain heretofore unexplored. Few if any MOF studies have considered that pore sizes smaller than electrolyte solvation diameters pose considerable energetic barriers to intercalation in comparison to surface-based redox. Furthermore, such distinct interior *vs* exterior redox behavior should become pronounced when the accessible surface of MOF exteriors and interiors become comparable, as with MOF nanocrystals.[23] Interestingly, MOF nanocrystals exhibit improved ion-transport dynamics in contrast to the bulk alternatives[24] and permit greater synthetic control over particle morphology and self-assembly,[24−28] opening fundamental investigations into structure−redox relationships. Conductive MOF nanocrystals with redox-active sites and nanoconfined pore environment therefore offer a unique platform for understanding intercalation chemistry in general.

Herein, we report the impact of nanoconfined pores on the ion-intercalation redox chemistry of Fe(TA)$_2$ (TA = 1,2,3-triazolate) MOF nanoparticles (Figure 1a,b). Due to the size mismatch between solvated BF$_4^-$ anions (ca. 10 Å in acetonitrile)[29] and the diameter of Fe(TA)$_2$ pores (ca. 4.54 Å),[30] an electrochemical potential of 1.2 V vs Fc$^{0/+}$ is required for the complete desolvation and intercalation of BF$_4^-$ anions (ca. 3 Å)[16] into the Fe(TA)$_2$ nanopore to drive Fe$^{2+}$/Fe$^{3+}$redox reactions. By comparison, at the exterior surface of the particles, the Fe$^{2+}$/Fe$^{3+}$ redox reactions, coupled with BF$_4^-$ adsorption, occur at ca. 0 V vs Fc$^{0/+}$. Although redox within the particles demands cooperative desolvation and intercalation, this exterior process only requires the partial desolvation of BF$_4^-$ anions and solvent reorganization akin to typical electrical double layers. Furthermore, controlling experimental factors (e.g., film thickness, electrolyte species, solvent, and reaction temperature) reveals that nanoconfinement leads to vastly different redox properties of ion-intercalation Fe$^{2+}$/Fe$^{3+}$ chemistry inside Fe(TA)$_2$ pores compared to the particle surface. In particular, a giant entropy change (i.e., ~160 J K$^{-1}$ mol$^{-1}$) accompanies the BF$_4^-$ intercalation redox chemistry within the Fe(TA)$_2$ pores that rivals the largest redox entropies of any known molecular or solid-state systems, and provides strategies for harnessing entropy to design electrochemical energy devices.

https://doi.org/10.1021/jacs.2c12846

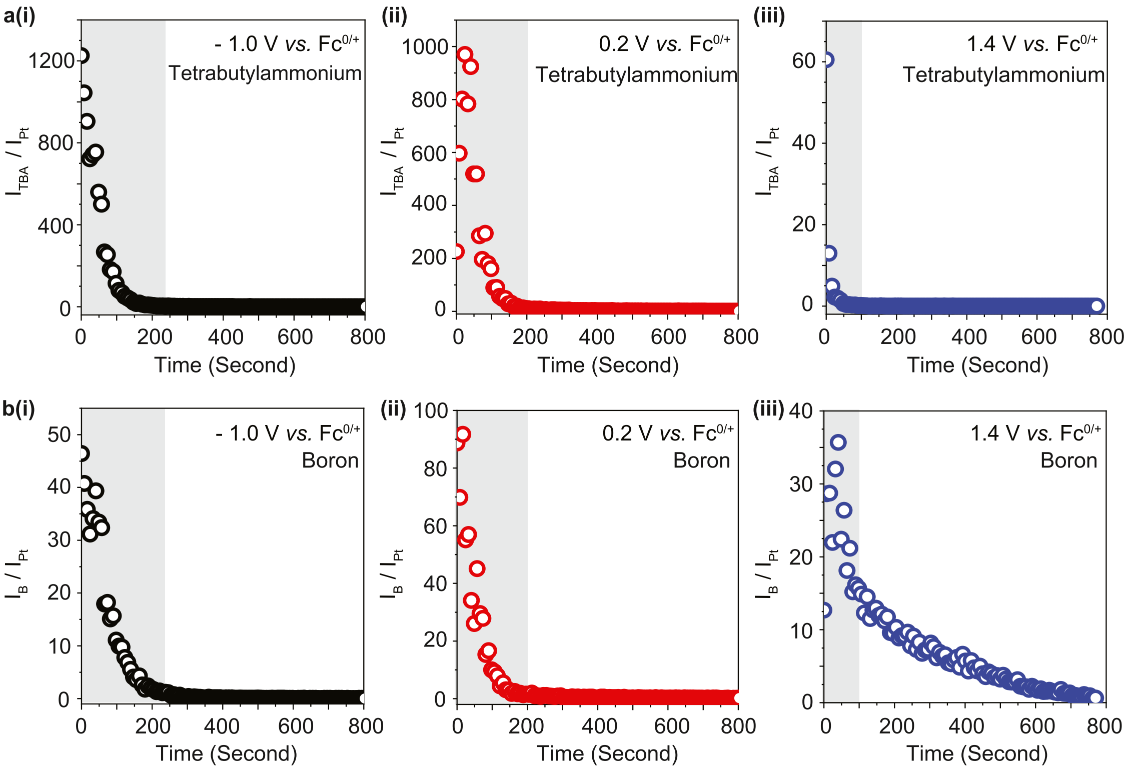

**Figure 3.** ToF-SIMS of spatial distribution of boron and $\text{TBA}^+$ cations in an $\text{Fe(TA)}_2$ film after applying different voltages. (a) ToF-SIMS depth profile of $\text{TBA}^+$ within $\text{Fe(TA)}_2$ film after applying (i) −1.0 V vs $\text{Fc}^{0/+}$, (ii) 0.2 V vs $\text{Fc}^{0/+}$, and (iii) 1.4 V vs $\text{Fc}^{0/+}$. (b) ToF-SIMS depth profile of boron within $\text{Fe(TA)}_2$ film after applying (i) −1.0 V vs $\text{Fc}^{0/+}$, (ii) 0.2 V vs $\text{Fc}^{0/+}$, and (iii) 1.4 V vs $\text{Fc}^{0/+}$. Both boron and $\text{TBA}^+$ signals are referenced to the Pt signal from the QCM crystal surface. The gray area represents the surface region of $\text{Fe(TA)}_2$ film that is defined by the spatial distribution of the $\text{TBA}^+$ signal. The spin-coating amount of 17-nm $\text{Fe(TA)}_2$ nanoparticles to those three EQCM electrodes was controlled to be ca. 5.5 $\mu$g (i.e., ca. 60 nm in film thickness) to obtain more depth-dependent data.

## ■ RESULTS AND DISCUSSION

**Identification of Intercalation vs Exterior Interfacial Redox Chemistry.** $\text{Fe(TA)}_2$ nanoparticles of varying sizes were synthesized following our recent work,[31] by adding different amounts of 1-methylimidazole as a "modulator" to the reaction mixtures (Figure 1c).[32] Scanning electron microscopy (SEM) analysis of the prepared materials indicated average nanoparticle sizes of ca. 17, 24, 41, and 83 nm (Figures 1c and S1, and DLS results in Table S1). Powder X-ray diffraction (PXRD) patterns of the nanoparticles confirmed they possessed the expected crystal structure of the low-spin $\text{Fe(TA)}_2$ phase (Figure S2). The recent study of $\text{Fe(TA)}_2$ nanocrystals reported cyclic voltammogram (CV) traces with multiple quasi-reversible features spanning more than a volt in electrochemical potential[32] and implied these originated from $\text{Fe}^{2+}/\text{Fe}^{3+}$ redox couples, despite the crystal structure suggesting all Fe sites exist in similar environments. If the large difference in potential stems from the small pores (ca. 4.54 Å in diameter)[30] creating distinct surface vs interior redox chemistry, $\text{Fe(TA)}_2$ offers a powerful platform for understanding intercalation redox chemistry inside the nanoconfined environment of porous materials.

Figures 2a and S3 show the CV trace of an $\text{Fe(TA)}_2$ film prepared by spin-coating ca. 4.0 $\mu$g of 17-nm nanoparticles onto a quartz crystal microbalance electrode. It exhibits multiple voltammetric features in the potential range from ca. −0.4 to 1.4 V vs $\text{Fc}^{0/+}$ with a notably sharp and reversible feature at ca. 1.2 V vs $\text{Fc}^{0/+}$, as reported previously.[31] Scanning between different potential windows confirms that the reversibility of this sharp feature corresponds to a distinct redox event independent of the others (Figure S4). In control studies, CV traces of a $\text{Zn(TA)}_2$ nanocrystal film (Figure S5) lacked redox signatures, confirming that the voltammetric features of $\text{Fe(TA)}_2$ films arise from $\text{Fe}^{2+}/\text{Fe}^{3+}$ redox events. Such large differences in electrochemical potential typically require significant alterations to a coordination sphere.[33] For instance, the $\text{Fe}^{2+}/\text{Fe}^{3+}$ redox potential occurs at ca. −0.7 V vs SCE in the tris-catecholate siderophore,[34] while the redox potential appears at ca. 1 V vs SCE for Fe centers coordinated with N-heterocyclic ligands phenanthroline or 2,2′-bipyridyl.[35] Accordingly, the ca. 1 V difference between the voltammetric features of the $\text{Fe(TA)}_2$ film suggests that despite crystallographically similar Fe sites, the $\text{Fe}^{2+}/\text{Fe}^{3+}$ redox waves must involve very different chemical environments.

Sharp and reversible "butterfly" signatures akin to double-peaked features in Figure 2a have been reported previously for CV traces of noble-metal electrodes, such as Pt. These sharp features have been attributed to disorder−order phase changes and other forms of solvent/electrolyte restructuring with surface adsorbates (e.g., $\text{SO}_{4\text{ads}}{}^{2-}$ or $\text{OH}_{\text{ads}}{}^{-}$ layers).[36] In these processes, the phase change of surface adsorbates maintains a constant mass since all species are already adsorbed. Accordingly, we monitored the potential-dependent mass variation of an $\text{Fe(TA)}_2$ film using in situ electrochemical quartz crystal microbalance (EQCM) electrodes. A significant mass increase and decrease were observable at the 1.2 V feature in the anodic and cathodic CV direction, respectively (Figures 2a and S6), excluding the possibility that the 1.2 V voltammetric feature is attributable only to a rearrangement of the absorbates on the Fe(TA)$_2$ film surface. It should be noted that no redox features at ca. 0 and 1.2 V are found on the blank EQCM electrode (Figure S7), excluding substrate interference and confirming that the redox features indeed originate from Fe(TA)$_2$ film. Additionally, we find that the current density of the 1.2 V voltammetric feature relates proportionally to (scan rate)$^{0.6}$ (Figure S8a,b). This scan rate dependence suggests that the redox event at ca. 1.2 V vs Fc$^{0/+}$ is mainly a diffusion-controlled process that requires the intercalation of anions into the film.[37] By comparison, the current density of the 0 V redox peak is proportional to (scan rate)$^{0.9}$ (Figure S8c), indicating that the 0 V voltammetric feature is a surface-adsorption-controlled process.

We further studied the mass change of the 1.2 V signature on the other three Fe(TA)$_2$ films prepared by spin-coating ca. 4.0 $\mu$g of 24-nm, 5.7 $\mu$g of 41-nm, and 0.7 $\mu$g of 83-nm nanoparticles onto the quartz crystal electrode, respectively (Figure S9). The mass increase at the 1.2 V feature (i.e., in the anodic scan direction) exhibits a linear relationship with the volume (Figure 2b) rather than the surface area of Fe(TA)$_2$ nanoparticles (Figure S10), confirming that the 1.2 V redox feature originates from the intercalation of electrolyte ions into Fe(TA)$_2$. Because the mass increase coincides with the redox feature, we propose that the intercalation occurs concomitantly with the Fe$^{2+}$/Fe$^{3+}$ redox event inside the nanoconfined pore environment. Similarly, as shown in Figure S11, the mass increase at the 0 V feature relates linearly with the volume of the nanoparticles. However, the slope of this relation for the 1.2 V feature is larger than the corresponding slope for the 0 V feature by a factor of ca. 6.4, consistent with the 1.2 V originating from events within the larger volume of the nanoparticle rather than the smaller volume of the Debye layer shell at the particle exterior. Therefore, these scaling relationships corroborate that the Fe$^{2+}$/Fe$^{3+}$ redox features in the potential range from ca. −0.4 to 0.2 V vs Fc$^{0/+}$ involve the adsorption of $BF_4^-$ anions on the Fe(TA)$_2$ surface, whereas the 1.2 V vs Fc$^{0/+}$ feature involves intercalation within the particles.

To further identify the origin of the 1.2 V feature, time-of-flight secondary ion mass spectrometry (ToF-SIMS) was employed to map the spatial distribution of both $BF_4^-$ anions and tetrabutylammonium (TBA$^+$) cations via sputtering through the Fe(TA)$_2$ film. Given that bulky TBA$^+$ cations cannot intercalate into the pore of Fe(TA)$_2$ nanoparticles, the spatial distribution of TBA$^+$ cations was used as the reference to identify the surface region of Fe(TA)$_2$ film in ToF-SIMS results (denoted as the gray area in Figure 3a(i,ii,iii)). After applying a potential of −1.0 V vs Fc$^{0/+}$ to Fe(TA)$_2$ film, the depth-dependent boron signal, originating from the bond cleavage of $BF_4^-$ anions during the surface sputtering, was only detected within the surface region (Figure 3b(i)). This result is consistent with the spatial distribution of TBABF$_4$ electrolyte under a negative applied potential, where both $BF_4^-$ anions and TBA$^+$ cations remain at the surface of the Fe(TA)$_2$ film. Furthermore, ToF-SIMS revealed a boron signal only in the surface region when applying 0.2 V vs Fc$^{0/+}$ to Fe(TA)$_2$ film (Figure 3b(ii)). This result indicates that the voltammetric Fe$^{2+}$/Fe$^{3+}$ features in the potential range from ca. −0.4 V to 0.2 V vs Fc$^{0/+}$ originate from the adsorption (anodic current) or desorption (cathodic current) of $BF_4^-$ anions at the exterior Fe sites. By contrast, after applying a potential of 1.4 V vs Fc$^{0/+}$, the boron signal was observable even at depths within the Fe(TA)$_2$ film (Figure 3b(iii)), confirming that the intercalation (anodic current) or deintercalation (cathodic current) of $BF_4^-$ anions into the Fe(TA)$_2$ pore indeed occurs at the 1.2 V Fe$^{2+}$/Fe$^{3+}$ redox feature. Further integration of the F and Fe features in X-ray photoelectron spectroscopy (XPS) shows that the ratio of F:Fe approaches 2:3 (Figure S12) after applying a potential of 1.4 V vs Fc$^{0/+}$ to the Fe(TA)$_2$ film. Because F only originates from $BF_4^-$ anions in the electrochemical system, we further use the F amount to quantify the boron content based on the stoichiometry of $BF_4^-$. This analysis provides an Fe:$BF_4^-$ ratio of ca. 1: 0.2, similar to the previously reported value (i.e., 1:0.33).[32]

The structural stability of an Fe(TA)$_2$ film cast onto an EQCM substrate was studied after redox cycling and $BF_4^-$ intercalation. Figure S13 and Table S2 show XRD data collected directly on a spin-coated Fe(TA)$_2$ film following electrochemical experiments. Although XRD intensities decrease compared to the powder signal due to the significant mass difference between film samples (ca. 4−5 $\mu$g) and powder samples (on the order of mg), we nevertheless observe the characteristic peak of Fe(TA)$_2$ at around 9° for the film sample. This XRD feature at around 9° remains for the Fe(TA)$_2$ film after the 6 cycles of CV scans, suggesting that the Fe(TA)$_2$ structure retains stability after redox cycles. Furthermore, the characteristic peak at 9° becomes less observable after holding the potential at 1.4 V vs Fc$^{0/+}$ for 30 min to achieve $BF_4^-$ intercalation. We propose that $BF_4^-$ intercalation distorts the Fe(TA)$_2$ structure, decreasing structural crystallinity and the XRD intensity. However, this structural distortion reverses, as evidenced by the increase of the XRD intensity of the Fe(TA)$_2$ characteristic feature at around 9° once $BF_4^-$ anions de-intercalate from the pore (i.e., XRD pattern of Fe(TA)$_2$ after CV in Figure S13b). This conclusion is corroborated by a previous study, where bulk Fe(TA)$_2$(BF$_4$)$_x$ ($x$ = 0, 0.09, 0.22, 0.33) displayed a similar XRD pattern of as-prepared Fe(TA)$_2$ after the chemical oxidation of Fe(TA)$_2$ with thianthrenium tetrafluoroborate.[32] Structural stability was also studied using ATR-FTIR performed directly on the Fe(TA)$_2$ film supported on the EQCM substrate after electrochemical experiments. Two vibrational features were detected at ca. 842 and 746 cm$^{-1}$ on the as-prepared Fe(TA)$_2$ film (Figure S14). According to our previous study,[38] these two vibrational features are assigned to C−H or N−N vibrational modes of the Fe(TA)$_2$, and observable following CV experiments and after holding the potential at 1.4 V vs Fc$^{0/+}$ for 30 min. We also found that the vibrational feature at 842 cm$^{-1}$ in the as-prepared Fe(TA)$_2$ film red-shifts to 839 cm$^{-1}$ after holding the voltage at 1.4 V vs Fc$^{0/+}$ for 30 min to allow $BF_4^-$ intercalation (Figure S14). Such a 3 cm$^{-1}$ vibrational shift suggests the change of chemical bonding in Fe(TA)$_2$, corroborating a structural distortion after $BF_4^-$ intercalation. Previous studies have reported BET surface areas for bulk Fe(TA)$_2$ and nanoparticles, where type II isotherm values of 336.5 m$^2$/g for bulk and 104.8 m$^2$/g for nanoparticles.[31,32] We expect that the surface area and unit cell volume of Fe(TA)$_2$ remain unchanged on the electrode support, due to the fact that the Fe(TA)$_2$ film is prepared by the spin-coating of nanoparticles onto the inert Pt substrates, rather than combining with a polymeric binder that could clog pore space, such as Nafion. Thermogravimetric analysis (TGA) was also performed and is plotted in Figure S15. It should be noted that similar two decomposition events were also reported previously for Fe(TA)$_2$(BF$_4$)$_{0.33}$.[32] As a control, Figure S15b shows that the decomposition temperature of TBABF$_4$ powder is ca. 352.5 °C, suggesting that the first event at ca. 238.8 °C for $Fe(TA)_2$ film after $BF_4^-$ encapsulation is attributable to the decomposition of $Fe(TA)_2$ film (Figure S15a). Taken together, these results suggest that $BF_4^-$ intercalation decreases the stability and crystallinity of $Fe(TA)_2$ films, but that this effect is reversible and similar to behavior in the bulk.

To test the explanation of ion-coupled charge transfer and distinct $Fe^{2+}/Fe^{3+}$ redox couples at the particle exterior and interior, we monitored mass changes and charge accumulation within the $Fe(TA)_2$ film. Specifically, as potentials sweep anodically the electrode mass should increase with $BF_4^-$ adsorption and intercalation to maintain charge balance. Indeed, Figures 2a and S16a show continuous mass increase and accumulation of positive charge within the $Fe(TA)_2$ film in the anodic CV direction. Interestingly, in contrast to the stark mass change observed in Figure 2a, the integrated charges exhibit a gradual increase without a significant change at the redox feature of 1.2 V vs $Fc^{0/+}$ (Figure S16b). Previous studies into metal oxides,[39] nanoporous carbon,[40] and 2D MXenes[41] demonstrate that the potential-dependent mass-to-charge ratios provide deep insight into the mechanism of ion intercalation. For instance, the apparent molecular mass ($M_w$') of a species can be measured by eq 1

$$M'_{w} = zF\left(\frac{\Delta m}{\Delta Q}\right) \tag{1}$$

where $z$ represents the number of electrons and $F$ is Faraday's constant. From $M_w$', the solvation number ($n$) of $BF_4^-$ anions involved during the intercalation/deintercalation process can be determined via eq 2

$$n = \frac{M'_{w} - M_{w}(BF_4^-)}{M_{w}(\text{solvent})} \tag{2}$$

where $M_w(BF_4^-)$ denotes the molecular weight of $BF_4^-$ anions and $M_w$(solvent) is the molecular weight of solvent (e.g., acetonitrile). If the $BF_4^-$ anions intercalate into $Fe(TA)_2$ nanopores without a solvation shell, the theoretical slope of $\frac{\Delta m}{\Delta Q}$ is ca. 0.9 (i.e., obtained under the assumption of $n = 0$ and $M_w = M_w(BF_4^-)$). Figure S4 shows that the "butterfly" intercalation feature at ca. 1.2 V vs $Fc^{0/+}$ consists of a prewave and a sharp peak. A similar feature has been observed at Pt surfaces, where the initial wave was assigned to surface electrolyte adsorption and the sharp peak was attributed to the disorder−order phase changes of adsorbates.[42,43] For the "butterfly" intercalation features of $Fe(TA)_2$ film ca. 1.2 V vs $Fc^{0/+}$, Figure 4 shows that the $\frac{\Delta m}{\Delta Q}$ slope in the initial region is ca. 0.5 (denoted as the orange line), smaller than the theoretical slope of 0.9. This result suggests that the initial feature arises from anion desolvation, while the sharp peak corresponds to $BF_4^-$ intercalation into the nanopores. Furthermore, the $\frac{\Delta m}{\Delta Q}$ slope of the sharp peak feature increases to ca. 1.0 (denoted as the red line in Figure 4). The similarity between the $\frac{\Delta m}{\Delta Q}$ value of the sharp feature and the theoretical slope (i.e., ca. 0.9) clearly demonstrates that $BF_4^-$ anions intercalate into the nanoconfined $Fe(TA)_2$ pores after complete desolvation. In addition, the $\frac{\Delta m}{\Delta Q}$ value for the $BF_4^-$ deintercalation redox (i.e., 1.2) is nearly identical to the ratio for intercalation redox (i.e., 1.0), further indication of a highly reversible $BF_4^-$ intercalation and deintercalation process also corroborated by mass variation in EQCM measurements (Figure S6). By comparison, the slope of $\frac{\Delta m}{\Delta Q}$ for the $BF_4^-$-adsorption-induced surface redox feature is ca. 0.2 (denoted as the green line in Figure 4), far below the theoretical value (i.e., 0.9). This analysis illustrates that when initially applying a positive electrochemical potential the adsorption of $BF_4^-$ anions also induces the desorption of solvents and $TBA^+$ cations from the $Fe(TA)_2$ film surface. On the other hand, the experimental $\frac{\Delta m}{\Delta Q}$ ratio for the $BF_4^-$-desorption-induced surface reactions equates to ca. 0.1, similar to the value of 0.2 for adsorption, likely due to the readsorption of $TBA^+$ cations and solvents to the $Fe(TA)_2$ film surface following desorption of $BF_4^-$ anions.

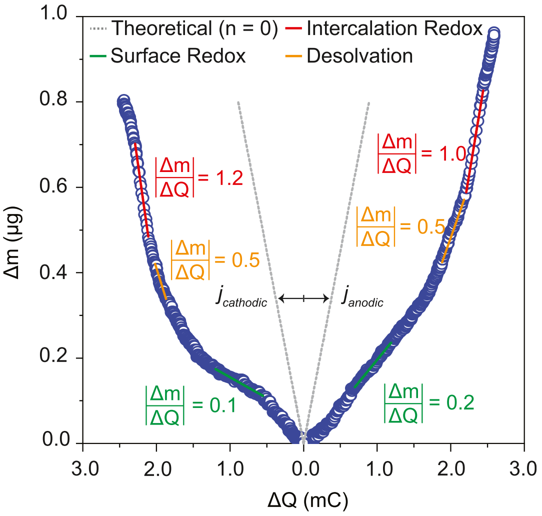

**Figure 4.** Film-thickness-dependent redox chemistry in $Fe(TA)_2$ film. (a(i)) AFM measurements of $Fe(TA)_2$ film prepared by spin-coating 4.0 μg of 16-nm nanoparticles, showing a film thickness of 21 ± 5 nm. (ii) Schematic of $BF_4^-$-induced surface and intercalation redox events within 21-nm-thick $Fe(TA)_2$ film. (iii) CV scans in a narrow potential window from −0.9 V to 0.3 V vs $Fc^{0/+}$. (iv) CV scans in a narrow potential window from 0.7 to 1.4 V vs $Fc^{0/+}$. (v) $\Delta E$ variation of intercalation redox feature in a 21-nm-thick $Fe(TA)_2$ film. (b(i)) AFM measurements of $Fe(TA)_2$ film prepared by loading 5.5 μg of 16-nm nanoparticles, showing the formation of a 60 ± 6 nm thickness film. (ii) Schematic of $BF_4^-$-induced surface and intercalation redox events within 60-nm-thick $Fe(TA)_2$ film. (iii) CV scans in a narrow potential window from −0.9 to 0.3 V vs $Fc^{0/+}$. (iv) CV scans in a narrow potential window from 0.7 to 1.4 V vs $Fc^{0/+}$. (v) $\Delta E$ variation of intercalation redox feature in a 60-nm-thick $Fe(TA)_2$ film. (c(i)) AFM measurements of $Fe(TA)_2$ film prepared by loading 4.0 μg of 25-nm nanoparticles, showing the formation of a 53 ± 8 nm thickness film. (ii) Schematic of $BF_4^-$-induced surface and intercalation redox events within 53-nm-thick $Fe(TA)_2$ film. (iii) CV traces in a narrow potential window from −0.9 to 0.3 V vs $Fc^{0/+}$. (iv) CV traces in a narrow potential window from 0.7 to 1.4 V vs $Fc^{0/+}$. (v) $\Delta E$ variation of intercalation redox feature in this 53-nm-thick $Fe(TA)_2$ film.

Taken together, the potential-dependent mass and charge variations and the electrochemical ToF-SIMS studies demonstrate that the voltammetric features in the range from ca. −0.4 to 0.2 V vs $Fc^{0/+}$ arise from surface $Fe^{2+}/Fe^{3+}$ oxidation triggered by the partial desolvation and adsorption of $BF_4^-$ anions to the $Fe(TA)_2$ film (Scheme 1a,b), whereas the voltammetric feature at 1.2 V vs $Fc^{0/+}$ originates from the $BF_4^-$-intercalation-induced $Fe^{2+}/Fe^{3+}$ redox chemistry in the

**Scheme 1. $BF_4^-$-Induced Surface and Intercalation Redox Chemistry in an $Fe(TA)_2$ Film. (a) $Fe(TA)_2$ Film in $TBABF_4$ Electrolyte in Acetonitrile under Open-Circuit Voltage (OCV). (b) $BF_4^-$-Induced $Fe^{2+}/Fe^{3+}$ Redox via the Partial Desolvation and Adsorption of $BF_4^-$ Anions on the Surface Fe Sites. (c) $BF_4^-$-Induced $Fe^{2+}/Fe^{3+}$ Redox Induced by the Complete Desolvation and Intercalation of $BF_4^-$ Anions into the Nanoconfined $Fe(TA)_2$ Pore**[a]

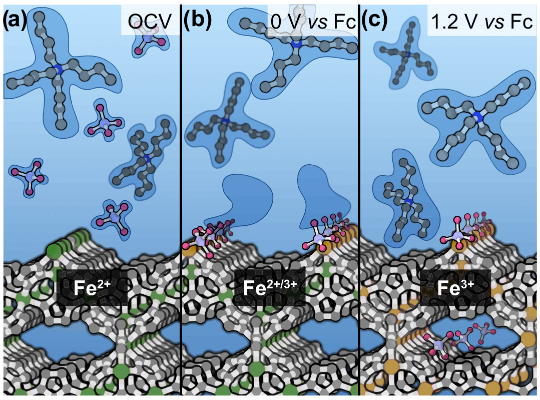

[a] Note: green, orange, gray, red, blue, and purple dots represent $Fe^{2+}$, $Fe^{3+}$, C, F, N, and B atoms, respectively. The blue cloud-shaped area represents the solvation shell of electrolyte ions.

nanopores of $Fe(TA)_2$ nanoparticles (Scheme 1(c)). Given that the solvated $BF_4^-$ anions (diameter of ca. 10 Å in acetonitrile) exceed the size of the $Fe(TA)_2$ cavity (diameter of ca. 4.54 Å), a large potential of 1.2 V vs $Fc^{0/+}$ is required to achieve the complete desolvation of $BF_4^-$ anions and to create a sufficient electrochemical potential across the film to drive intercalation of desolvated $BF_4^-$ anions (diameter of ca. 3 Å) into the nanoconfined pores.

To begin unraveling the complex supramolecular chemistry involved in the intercalation process, we conducted DFT calculations using the climbing image nudged elastic band (CI-NEB) method to understand energetic barriers of $BF_4^-$ anions moving between nanopores in $Fe(TA)_2$. Notably, $BF_4^-$ surrounded by solvent molecules far exceeds the pore sizes and thus could not be modeled. We calculated an intercalation energy of −116.23 kcal/mol, indicating a highly stable intercalated complex. When using continuum dielectric (implicit solvent) model, we found an activation barrier of $BF_4^-$ intercalation from one nanopore to another of ca. 19.28 kcal/mol or ca. 0.84 eV. When calculated in vacuum, a similar intercalation energy barrier (i.e., 20.22 kcal/mol or ca. 0.87 eV) was determined. The full computed energetic profile and representative structures of initial, transition, and final states are included in Figure S17. This large energy barrier of 0.84 eV further supports our claim that the redox feature at 1.2 V vs $Fc^{0/+}$ arises from additional electrochemical potential required to drive the intercalation of $BF_4^-$ anions into the nanoconfined $Fe(TA)_2$ pores.

**Factors Controlling Anion Intercalation Redox Chemistry within $Fe(TA)_2$ Nanopores.** To study the impact of interparticle and inner-particle diffusion on the anion-coupled redox processes of $Fe(TA)_2$, films of varying thickness and particle sizes were investigated by first spin-coating ca. 4.0 μg of 17-nm $Fe(TA)_2$ nanoparticles onto a quartz crystal electrode. Atomic force microscopy (AFM) indicates that the nanoparticles self-assemble into a film with a thickness of ca. 21 ± 5 nm (Figure 5a(i)), suggesting the formation of monolayer $Fe(TA)_2$ films (Figure 5a(ii)). CV traces of this $Fe(TA)_2$ film were collected in narrow potential windows to isolate the surface and ion-intercalation redox features. Repeated cycles of this monolayer film showed unchanging current densities and peak-to-peak separations ($\Delta E$) for both the surface and ion-intercalation redox features (Figure 5a(iii,iv)), indicating good kinetic reversibility. Increasing the spin-coating mass of 17-nm $Fe(TA)_2$ nanoparticles to 5.5 μg led to an $Fe(TA)_2$ film with a thickness of 60 ± 6 nm (Figure 5b(i)), which corresponds to ca. four-particle layers (Figure 5b(ii)). Although the surface redox reaction feature exhibits kinetic reversibility (Figure 5b(iii)), the intercalation chemistry at 1.2 V vs $Fc^{0/+}$ gradually becomes sluggish as evidenced by the increase of $\Delta E$ (from ca. 49 to 58 mV) in the CV scans (Figure 5b(iv)). This increase in $\Delta E$ together with the current density decrease of the 1.2 V redox feature illustrates that increasing the film thickness hinders the intercalation and deintercalation dynamics of $BF_4^-$ anions, and further suppresses the ion-intercalation redox reactions inside the nanoconfined pore environment.

To explore the effect of particle size on the kinetics of intercalation chemistry, a 53 ± 8-nm-thick $Fe(TA)_2$ film (i.e., ca. two-particle layers) was prepared by loading ca. 4.0 μg of 24-nm $Fe(TA)_2$ nanoparticles onto the quartz crystal electrode (Figure 5c(i,ii)). As shown in Figures 5c(iii) and S19, the use of larger 24-nm nanoparticles left the thermodynamic (i.e., $E_{1/2}$) and kinetic properties (i.e., $\Delta E$) of the surface redox reactions unchanged. By contrast, a more significant current density decrease and $\Delta E$ increase (i.e., from ca. 84 to 132 mV) were detected for the $BF_4^-$-intercalation redox feature (Figure 5c(iv)) compared to the changes observed for a similar thickness film made from 17-nm $Fe(TA)_2$ nanoparticles. We attribute this size effect to the $BF_4^-$ traveling farther distances in the nanoconfined environment of the 24-nm nanoparticles (Figure 5c(ii)) compared to the shorter distances within a similar thickness film formed by more assembled 17-nm-nanoparticle layers, where more interparticle space exists for the $BF_4^-$ intercalation (Figure 5b(ii)). A longer inner-particle intercalation pathway could lead to sluggish intercalation and deintercalation dynamics of $BF_4^-$ anions and severely hinder the intercalation redox reaction inside the film made by 24-nm $Fe(TA)_2$ nanoparticles. Taken together, these studies illustrate that the mass transport of $BF_4^-$ anions into $Fe(TA)_2$ has a more significant impact on the intercalation redox feature at 1.2 V vs $Fc^{0/+}$ compared to the surface redox when increasing the $Fe(TA)_2$ film thickness since $BF_4^-$ anions remain accessible to surface Fe sites regardless of the film thickness.

Given that the small pore sizes of $Fe(TA)_2$ impose a large electrochemical barrier to redox at the interior Fe sites, the impact of electrolyte identity was explored. While keeping $BF_4^-$ as the counter anion, replacing $TBA^+$ cations with the smaller trimethylamine ($TMA^+$) cations induced a positive shift of the intercalation redox feature from 1.23 V vs $Fc^{0/+}$ to 1.27 V vs $Fc^{0/+}$ and a positive shift for the surface redox features from 0.02 V vs $Fc^{0/+}$ in $TBABF_4$ to 0.04 V vs $Fc^{0/+}$ in $TMABF_4$ (Figure 6a). We interpret these cation-dependent electrochemical studies as demonstrating that strong ion pairing between cations and $BF_4^-$ anions hinders the ion intercalation and the corresponding redox reactions of the $Fe(TA)_2$ film. Furthermore, the use of $LiBF_4$ as the electrolyte greatly reduced the current density of both intercalation and surface redox features (Figure 6a). In addition to the intense

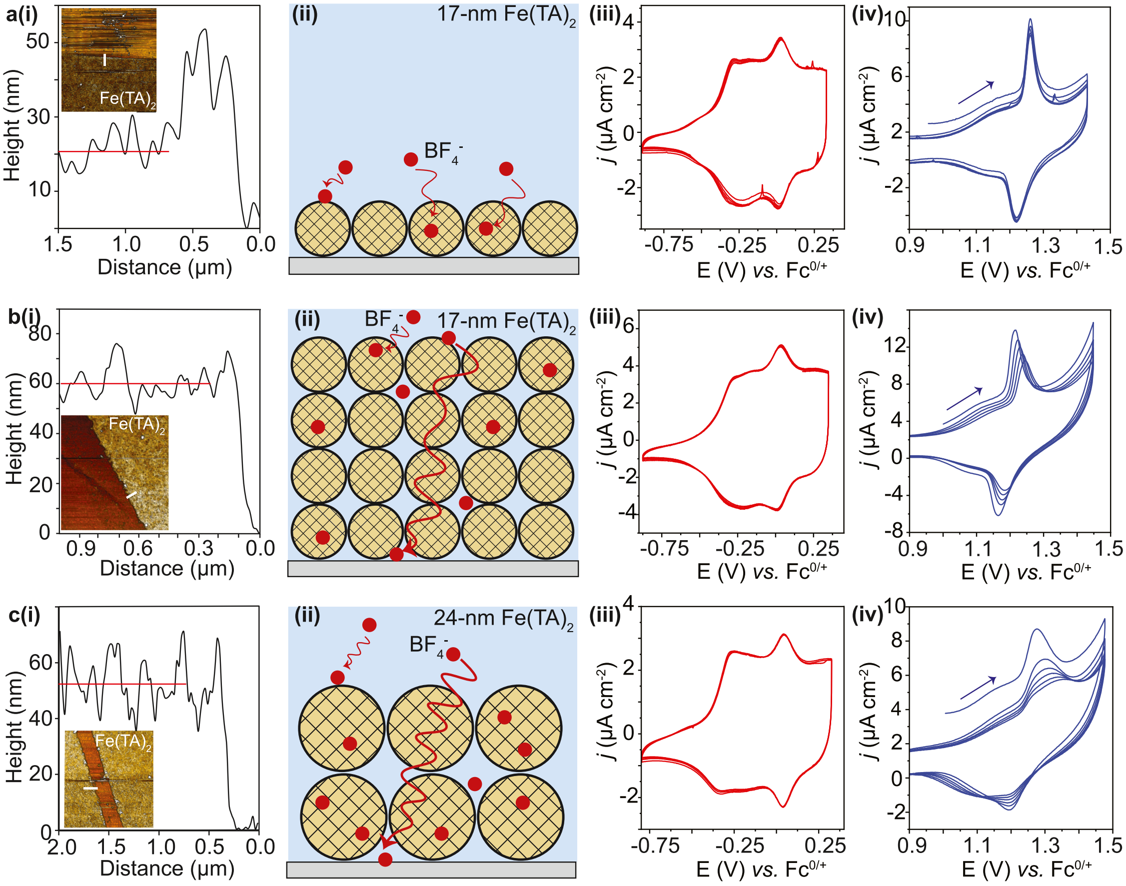

**Figure 5.** Film-thickness-dependent redox chemistry in an Fe(TA)$_2$ film. (a(i)) AFM measurements of Fe(TA)$_2$ film prepared by spin-coating 4.0 μg of 17-nm nanoparticles, showing a film thickness of 21 ± 5 nm. (ii) Schematic of BF$_4^-$-induced surface and intercalation redox events within 21-nm-thick Fe(TA)$_2$ film. (iii) CV scans in a narrow potential window from −0.9 to 0.3 V vs Fc$^{0/+}$. (iv) CV scans in a narrow potential window from 0.9 to 1.5 V vs Fc$^{0/+}$. (b(i)) AFM measurements of Fe(TA)$_2$ film prepared by spin-coating 5.5 μg of 17-nm nanoparticles, showing a film thickness of 60 ± 6 nm. (ii) Schematic of BF$_4^-$-induced surface and intercalation redox events within 60-nm-thick Fe(TA)$_2$ film. (iii) CV scans in a narrow potential window from −0.9 to 0.3 V vs Fc$^{0/+}$. (iv) CV scans in a narrow potential window from 0.9 to 1.5 V vs Fc$^{0/+}$. (c(i)) AFM measurements of Fe(TA)$_2$ film prepared by loading 4.0 μg of 24-nm nanoparticles, showing the formation of a 53 ± 8 nm thickness film. (ii) Schematic of BF$_4^-$-induced surface and intercalation redox events within 53-nm-thick Fe(TA)$_2$ film. (iii) CV traces in a narrow potential window from −0.9 to 0.3 V vs Fc$^{0/+}$. (iv) CV traces in a narrow potential window from 0.9 to 1.5 V vs Fc$^{0/+}$.

ion pairing between the smallest Li$^+$ cations and BF$_4^-$ anions, Li$^+$ may also chemisorb on Fe(TA)$_2$ and thereby prevent the adsorption/intercalation of BF$_4^-$ to redox-active Fe centers. EQCM measurements with LiBF$_4$ display a mass decrease in the anodic CV direction before both surface and intercalation redox features (Figure S20). We propose that such a mass decrease is mainly attributable to the Li$^+$ desorption from the Fe(TA)$_2$ film. The desorption of Li$^+$ frees a portion of the Fe centers, allowing the adsorption/intercalation of BF$_4^-$ anions to trigger the Fe$^{2+/3+}$ redox chemistry in Fe(TA)$_2$, which is evidenced by the redox wave and the mass increase that occur after the Li$^+$-desorption-induced mass decrease (Figure S20). Overall, the significantly reduced current density of both intercalation and surface redox features when using LiBF$_4$ as electrolytes suggests that only small amounts of Li$^+$ can be released from Fe(TA)$_2$, while the majority of Fe centers are still "poisoned" by strongly bonded Li$^+$ cations.

Similarly, we explored the impact of anion size in relation to the Fe(TA)$_2$ nanoparticle pore size in controlling the intercalation redox chemistry. Given the comparable size between desolvated BF$_4^-$ anions (ca. 3 Å in diameter) and the cavity of Fe(TA)$_2$ nanoparticles (ca. 4.5 Å in diameter), BF$_4^-$ anions can intercalate into the nanoconfined pores under the sufficient electrochemical potential (ca. 1.2 V vs Fc$^{0/+}$). Instead, we found that when employing the larger ClO$_4^-$ anions (ca. 4.8 Å in diameter) the current density greatly reduces at the ion-intercalation redox feature compared to the surface redox features (Figure 6b), suggesting that the intercalation process becomes blocked if electrolyte ions exceed the size of the Fe(TA)$_2$ nanopores. Indeed, the use of the even larger PF$_6^-$ anions (ca. 5.0 Å in diameter) as electrolytes causes this ion-intercalation redox feature to completely disappear (Figure 6b). The disappearance of the intercalation redox feature induced by replacing the BF$_4^-$ anions with the larger PF$_6^-$ anions while keeping TBA$^+$ constant as the counter cations demonstrates that the 1.2 V redox feature in Fe(TA)$_2$ voltammograms originates from the intercalation/deintercalation of anions rather than TBA$^+$ cations. In addition to the intercalation redox feature, the surface Fe$^{2+}$/Fe$^{3+}$ redox reactions at ca. 0 V vs Fc$^{0/+}$ also exhibit anion (e.g., BF$_4^-$, PF$_6^-$, ClO$_4^-$, Br$^-$ and Cl$^-$)-dependent behavior (Figures 6b and S21). In a previous capacitance study, the double-layer structure of the Pt(111)-aqueous electrolyte interface was shown to depend on the electrolyte identity.[44] Accordingly, we propose that the anion-dependent changes to the ca. 0 V vs Fc$^{0/+}$ features arise from

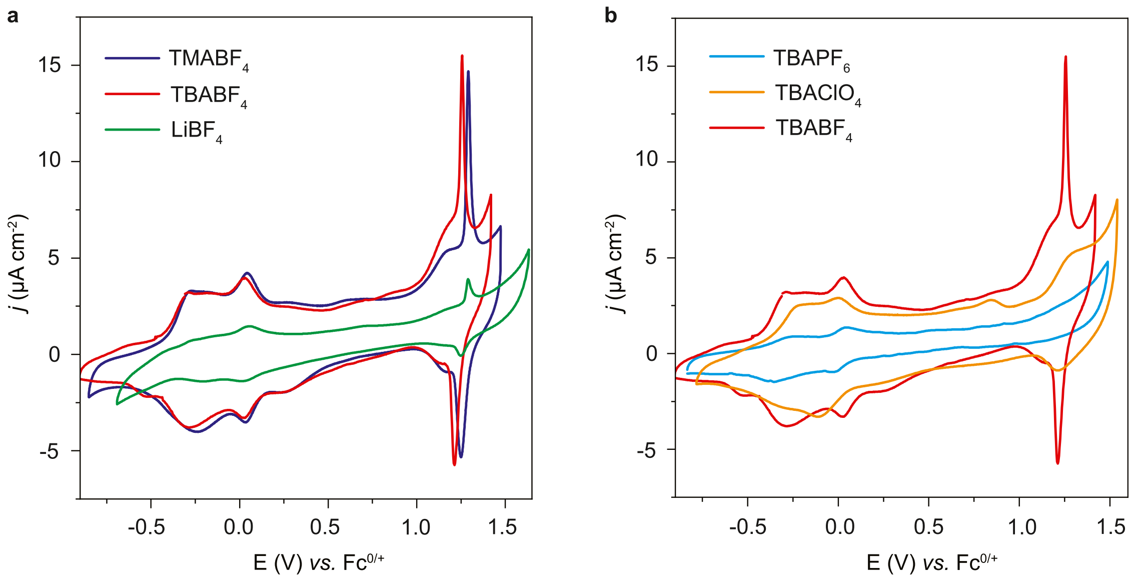

**Figure 6.** Electrolyte-dependent electrochemical studies of Fe(TA)$_2$ nanoparticle film. (a) Cation-dependent CV measurements of 17-nm Fe(TA)$_2$ nanoparticle film. (b) Anion-dependent CV measurements of 17-nm Fe(TA)$_2$ nanoparticle film. Note: CV scan is collected at a 10-mV/s scan rate in acetonitrile and the electrolyte concentration is 0.1 M. The loading amount of 17-nm Fe(TA)$_2$ nanoparticle is controlled to be ca. 4.0 $\mu$g on QCM crystals.

distinct double-layer structures at the Fe(TA)$_2$ surface—electrolyte interface, altering the interaction between anions and surface Fe sites and leading to the ion-specific surface redox chemistry.

To probe the anion effect further, small quantities of TBAPF$_6$ (i.e., mM scale) were titrated into a 0.1 M TBABF$_4$ electrolyte solution containing a 17-nm Fe(TA)$_2$ nanoparticle film. Figure 7a shows that even small additions of PF$_6^-$ hindered intercalation-based redox inside the Fe(TA)$_2$ nanopores, evidenced by the continuous decrease of current density at 1.2 V vs Fc$^{0/+}$. In addition, the $\Delta E$ of BF$_4^-$-intercalation redox feature also increased to a greater degree than the $\Delta E$ increase of the surface redox features, indicating sluggish BF$_4^-$ intercalation dynamics in the presence of the larger PF$_6^-$anions (Figure S22). A similar "poisoning effect" on ion-intercalation redox chemistry in Fe(TA)$_2$ film was also observable by titrating small amounts of TBAClO$_4$ into the TBABF$_4$ electrolyte solution (Figure S23). These titration experiments suggest that the presence of larger PF$_6^-$ and ClO$_4^-$ anions blocks BF$_4^-$ intercalation into the nanoconfined pore of Fe(TA)$_2$ particles and therefore suppresses the intercalation redox chemistry. Indeed, EQCM detected a more severe mass decrease at the intercalation redox feature at 1.2 V vs Fc$^{0/+}$ compared to the mass decrease at a surface redox feature around 0 V vs Fc$^{0/+}$ (Figure 7b). The blocking effect of larger PF$_6^-$ anions on the BF$_4^-$ intercalation further hinders the ion-coupled charge transport for Fe$^{2+}$/Fe$^{3+}$ redox events inside the nanoconfined pores as evidenced by the continuous decrease of charges accumulated at the intercalation redox feature (Figure 7b). Furthermore, electrochemical impedance spectroscopy (EIS) was utilized to probe fundamental aspects of the charge transfer and the mass transport in BF$_4^-$-intercalation-induced Fe$^{2+}$/Fe$^{3+}$ redox event. EIS spectra were collected on a 17-nm nanoparticle Fe(TA)$_2$ film after each titration step (Figure 7c). The data were fitted to a parallel combination of the capacitance and the charge transfer resistance with a finite-space Warburg, as has been used to model ion transportation in porous materials.[45] The fitting results indicate a significant increase in the ion-transport resistance ($R_d$) compared to the charge transport ($R_{ct}$) by titrating PF$_6^-$ anions into a BF$_4^-$ electrolyte mixture with an Fe(TA)$_2$ film (Figure 7d). This EIS study confirms that the continuous decrease of intercalation redox current in titration experiments originates from the PF$_6^-$-anion-induced sluggish BF$_4^-$ intercalation dynamics into nanoconfined Fe(TA)$_2$ pores. Taken together, titration experiments along with anion-size-dependent and film-thickness-dependent investigations together illustrate that the mass transport of anions defines the rate-determining step of Fe$^{2+}$/Fe$^{3+}$ redox reaction inside nanoconfined Fe(TA)$_2$ pores.

Given the importance of desolvation to the BF$_4^-$-intercalation-induced redox chemistry and BF$_4^-$-adsorption-induced surface reactions, we investigated the impact of solvent identity on the redox properties of an Fe(TA)$_2$ film. In addition to acetonitrile, CV traces were collected for an Fe(TA)$_2$ film in 1,2-difluorobenzene. Since 1,2-difluorobenzene is a chemically inert and noncoordinating solvent,[46] we expected that lower potentials would be required to drive the complete desolvation and intercalation of BF$_4^-$ anions into the Fe(TA)$_2$ pore compared to acetonitrile. Indeed, Figure S24 shows a ca. 150-mV cathodic shift of $E_{1/2}$ of BF$_4^-$-intercalation redox reaction inside the Fe(TA)$_2$ nanopores when using 1,2-difluorobenzene. Since the potential of ca. 1.2 V vs Fc$^{0/+}$ exceeds the potential window of many commonly used solvents, we focused our study of solvent effects on the surface redox properties of Fe(TA)$_2$ film at ca. 0 V vs Fc$^{0/+}$. As with the intercalation redox reaction, the $E_{1/2}$ of the BF$_4^-$-adsorption-induced Fe$^{2+}$/Fe$^{3+}$ redox feature also shifts cathodically by switching acetonitrile to 1,2-difluorobenzene (Figure S25). Interestingly, as summarized in Figure S25, the surface redox features were highly dependent on all studied solvents (e.g., acetonitrile, dichloromethane, tetrahydrofuran, and 1,2-difluorobenzene) as evidenced by different $E_{1/2}$ and current densities. We hypothesize that distinct solvents with different dielectric constants and donor abilities alter the structure of the electric double layer on the Fe(TA)$_2$ film surface, impacting

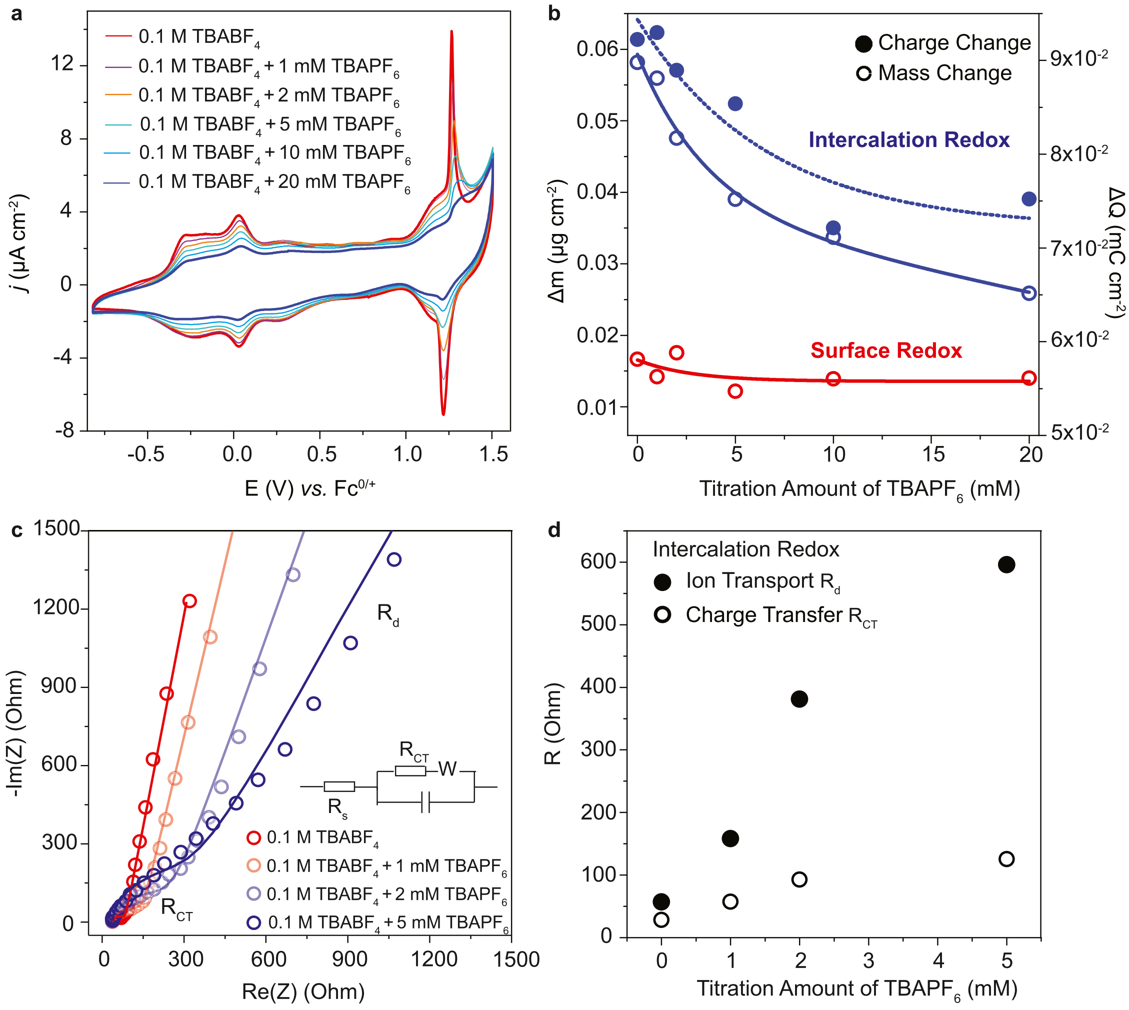

**Figure 7.** Electrolyte-dependent redox properties in an $Fe(TA)_2$ nanoparticle film. (a) CV measurements of a 17-nm $Fe(TA)_2$ nanoparticle film during titrating $TBAPF_6$ into a 0.1 M $TBABF_4$ acetonitrile electrolyte. (b) Mass (hollow circle) and charge (solid circle) changes of a 17-nm $Fe(TA)_2$ nanoparticle film during titrations of $TBAPF_6$ into a 0.1 M $TBABF_4$ acetonitrile electrolyte. (c) Nyquist plot of ion-intercalation redox chemistry within an $Fe(TA)_2$ film during titration experiments at an applied potential of intercalation redox feature. $R_{CT}$ represents the charge transfer resistance. W stands for the finite-space Warburg element used to model the behavior of ion transport within MOFs in the low-frequency region of the impedance spectra. Ion-transport resistance, $R_d$, is obtained from the finite-space Warburg. The frequency of EIS measurements spanned from 4.5 kHz to 60 mHz. (d) Change of charge-transfer and ion-transport resistances of ion-intercalation redox chemistry within $Fe(TA)_2$ film during titration experiments. Note: the loading amount of 17-nm $Fe(TA)_2$ nanoparticles is controlled to be ca. 4.0 $\mu g$ on QCM crystals.

the adsorption of $BF_4^-$ anions on surface Fe sites and leading to the solvent-dependent $Fe^{2+}/Fe^{3+}$ redox features. Overall, our studies confirm that the solvent identity serves as a critical factor in the microscopic picture of both surface reactions and the ion-intercalation redox chemistry inside the nanoconfined $Fe(TA)_2$ pores.

**Redox Entropy of Anion Intercalation within Nanoconfined $Fe(TA)_2$ Pores.** Large changes in entropy often accompany redox reactions within electrodes coupled to ion intercatalation,[47] which can be measured using the following equation

$$\frac{\partial E}{\partial T} = \frac{\Delta S}{nF} \tag{3}$$

where $\frac{\partial E}{\partial T}$ is the temperature coefficient, $E$ is the equilibrium voltage, $T$ is the temperature, $n$ is the number of charges participating in the reaction, $F$ is Faraday's constant, and $\Delta S$ is the entropy change of reaction (see the SI for detailed equations and parameters). Accordingly, CV traces of an $Fe(TA)_2$ film using $TBABF_4$ as electrolytes in acetonitrile were recorded under variable-temperature conditions. Figure 8a shows that increased temperatures induce an anodic shift of $E_{1/2}$ for the $BF_4^-$-intercalation redox feature, corresponding to a temperature coefficient and entropy change of 1.7 ± 0.2 mV/K (Figure 8c) and ca. 164 J $K^{-1}$ $mol^{-1}$, respectively. In contrast, $E_{1/2}$ of the surface redox feature shifts in the cathodic direction with increasing temperature (Figure 8b). The corresponding temperature coefficient and the entropy change were −0.7 ± 0.2 mV/K (Figure 8c) and −67.6 J $K^{-1}$ $mol^{-1}$, respectively.

The opposite signs of reaction entropy and the temperature-dependent $E_{1/2}$ variation suggest distinct behaviors between the intercalation redox reaction inside the nanopores and the redox chemistry at the $Fe(TA)_2$ film surface. The anodic shift of $E_{1/2}$ for intercalation-based redox suggests that the increase of reaction temperature disfavors the oxidation of $Fe^{2+}$ to $Fe^{3+}$ inside the nanopores. Given that Figures 4 and 5 suggest the mass transport of $BF_4^-$ into the nanoconfined pores dominates the rate-determining step and that $BF_4^-$ intercalation occurs

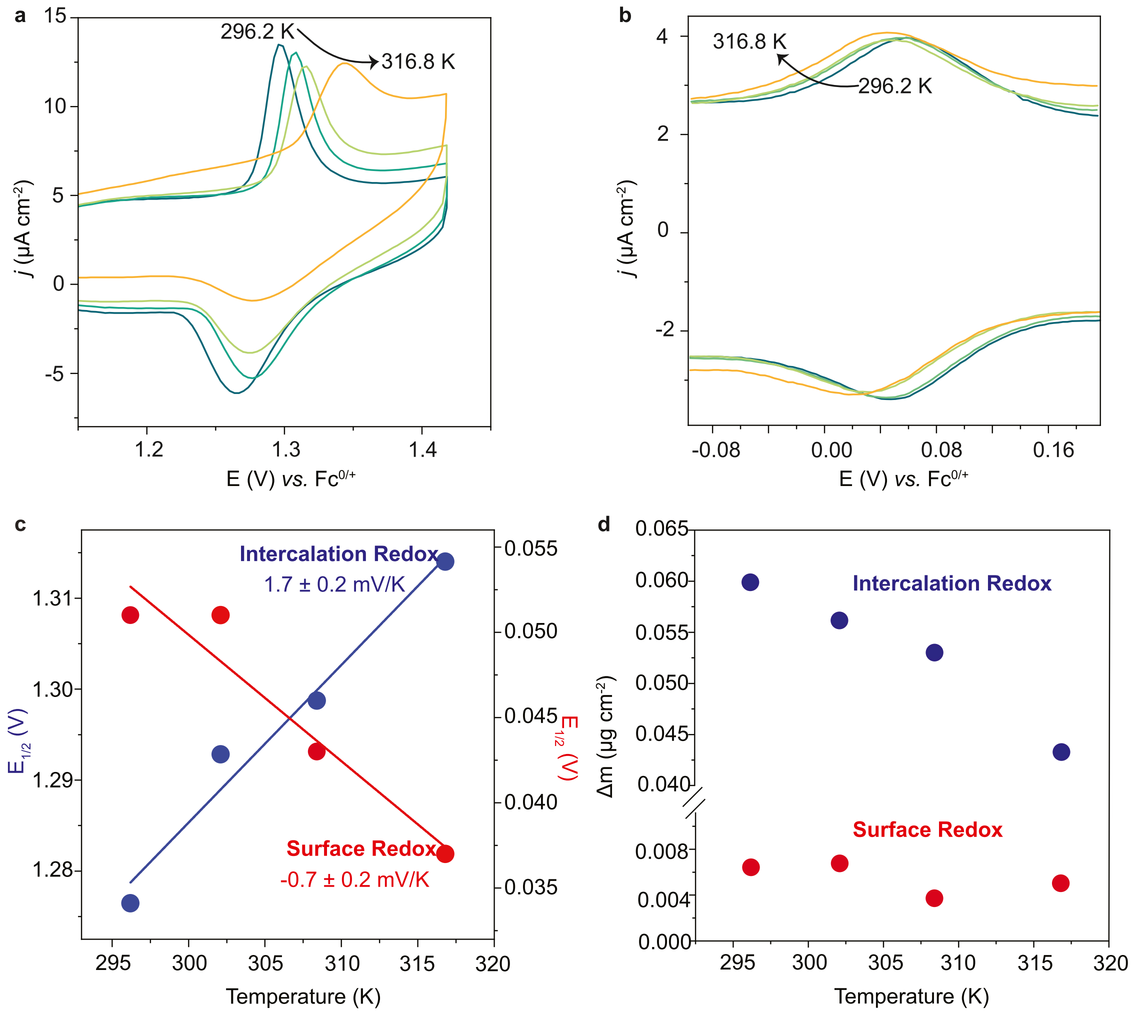

**Figure 8.** Temperature-dependent redox properties of an Fe(TA)$_2$ film. (a) Temperature-dependent CV of a 17-nm Fe(TA)$_2$ film, showing the change in the redox feature at 1.2 V vs Fc$^{0/+}$. (b) Temperature-dependent CV traces of a 17-nm Fe(TA)$_2$ film, showing the change of the redox feature at 0 V vs Fc$^{0/+}$. Note: CV scans were collected at a 10-mV/s scan rate in 0.1 M TBABF$_4$ in acetonitrile. The loading amount of 17-nm Fe(TA)$_2$ nanoparticle was controlled to be ca. 4.0 $\mu$g on EQCM crystals. (c) Temperature-dependent $E_{1/2}$ variation of both intercalation redox and surface redox reactions for a 17-nm Fe(TA)$_2$ film. (d) Temperature-dependent mass change of both surface redox and intercalation reactions for a 17-nm Fe(TA)$_2$ film.

after desolvation ($n$ = 0), we monitored the temperature-dependent mass changes to Fe(TA)$_2$ films at the intercalation redox feature. A continuous mass decrease and an increase of mass transport (i.e., $BF_4^-$ intercalation) resistance were detected with increased reaction temperatures (Figures 8d and S26), suggesting that higher temperatures suppress the intercalation of $BF_4^-$ anions into the Fe(TA)$_2$ nanopores. A possible contributing factor could be that enhanced metal—ligand dynamic bonding at elevated temperatures[38,48] might induce additional phonon scattering that interferes with $BF_4^-$ intercalation. According to an ion-coupled charge transport mechanism, a hindered $BF_4^-$ intercalation step should also prevent the charge transfer process. Indeed, EIS data indicate that raising the reaction temperature significantly increases the charge transfer resistance (Figure S26), confirming that the reduced $BF_4^-$ intercalation prevents the charge transfer to drive $Fe^{2+}/Fe^{3+}$ redox chemistry inside the Fe(TA)$_2$ nanopores. As a result, a more positive applied potential is required to further drive the $BF_4^-$ intercalation to trigger $Fe^{2+}/Fe^{3+}$ redox reaction inside the nanoconfined Fe(TA)$_2$ pores when increasing the reaction temperature (Figure 8a). On the other hand, the insertion of $BF_4^-$ from the electrolyte into the nanoconfined MOF channels involves a huge reduction in the number of microstate configurations, suggesting that the intercalation of $BF_4^-$ is an entropically disfavored process. Given the increase of temperature hinders the intercalation process, more $BF_4^-$ anions remain in the electrolyte, due to the far greater density of microstates when solvated, leading to a giant positive reaction entropy change. Similar entropy changes have been reported previously in lithium- and sodium-ion batteries during the ion-intercalation step.[47,49,50]

By comparison, raising the temperature did not cause an obvious mass decrease (Figure 8d) at the surface redox features, thereby excluding $BF_4^-$ desorption as the origin of the cathodic shift of $E_{1/2}$. Previous reports have shown that acetonitrile solutions exhibit strong layering and orientational ordering in the electric double layer at electrode—electrolyte interfaces.[29] Accordingly, we propose that acetonitrile partially desolvates from $BF_4^-$ anions during the surface $Fe^{2+}/Fe^{3+}$ redox event to create a more well-ordered electric double layer at the nanocrystal exterior. This solvent-electrolyte ordering at the Fe(TA)$_2$—electrolyte interface leads to a negative redox entropy (Figure 8c). Meanwhile, EIS data indicate that elevated temperatures reduce the resistance of $BF_4^-$ transport from the bulk electrolyte to surface Fe sites of $Fe(TA)_2$ film (Figure S27). This result corroborates the microscopic picture that $BF_4^-$ anions more easily access surface Fe sites to facilitate $Fe^{2+}/Fe^{3+}$ redox chemistry, leading to a cathodic shift of $E_{1/2}$ of the surface redox feature at higher temperatures (Figure 8b).

## OUTLOOK AND CONCLUSIONS

In future studies, surface-specific spectroscopic methods in combination with computational methods will unravel the complex supramolecular chemistry governing the electrolyte restructuring and adsorption at the $Fe(TA)_2$ external and internal surfaces. Given the unique feature of $Fe(TA)_2$ possessing different forms of "surface", such studies into $Fe(TA)_2$ nanoparticles will provide general insight into anion-dependent and solvent-dependent surface redox chemistry. In situ electrochemical X-ray absorption spectroscopy (e.g., EXAFS and EXANS) and Raman investigations will also prove useful in understanding the influence of metal−ligand reversible bonding[38,48] and the evolution of structural defects in $Fe(TA)_2$ nanoparticles during the ion-intercalation redox chemistry. Furthermore, because the nanoconfinement-induced complete desolvation of $BF_4^-$ minimizes the distance between $BF_4^-$ and interior $Fe(TA)_2$ surface sites, we anticipate promising pseudo-capacitance behavior from $Fe(TA)_2$ nanoparticles. Indeed, preliminary measurements indicate performance comparable to recent MOF electrodes (Figure S28).[1,4] The giant redox entropy of $Fe(TA)_2$ nanoparticle films provides a roadmap for expanding voltage windows of batteries and other energy storage devices without altering the composition of the electrode, and for designing thermoelectric materials as Seebeck coefficients depend proportionally on entropy. In addition, realizing the full potential of MOFs as intercalation materials will involve guest molecules with properties that enhance the behavior of the parent MOF. For example, metallacarboranes with high robustness, the ability to accommodate metal atoms, electron-delocalized skeletal bonding, and superchaotropic behavior have been utilized as guest molecules to manipulate MOF properties. For instance, nickel(IV) bis(dicarbollide) was incorporated in a zirconium-based NU-1000 MOFs to improve the electrical conductivity.[51] Lithium cobalt(III) bis(dicarbollide) was also incorporated in a MIL53(Al) framework to enhance Li-ion conductivity.[52] Future efforts will focus on integrating metallacarboranes and other next-generation ions as guest molecules into nanoconfined pores to further manipulate and improve the electrochemical properties of MOFs for energy applications and storage.

In summary, these results illustrate that nanoconfined environments govern the ion-intercalation redox chemistry of $Fe(TA)_2$ nanoparticles. The gating effect of pores smaller than solvated electrolyte requires additional electrochemical potentials exceeding one volt to drive the complete desolvation and the intercalation of $BF_4^-$ anions into the pore compared to the partial desolvation and adsorption of $BF_4^-$ anions on the $Fe(TA)_2$ surface. The further manipulation of experimental factors (e.g., film thickness, electrolyte species, solvents, and the reaction temperature) reveal that the redox properties of ion intercalation into the nanoconfined environment of $Fe(TA)_2$ pores differ from the surface redox reactions, despite all Fe sites being crystallographically similar. The mass transport of $BF_4^-$ anions determines the kinetic and thermodynamic aspects of $Fe^{2+}/Fe^{3+}$ redox chemistry inside the $Fe(TA)_2$ nanopores, while the surface $Fe^{2+}/Fe^{3+}$ redox depends strongly on solvent and electrolyte identity. As a quantitative metric of the nanoconfinement effect, a giant entropy (i.e., 164 J $K^{-1}$ $mol^{-1}$) is observed for the $BF_4^-$-intercalation-induced $Fe^{2+}/Fe^{3+}$ redox reaction, due to the cooperative desolvation and intercalation of $BF_4^-$ anions. These fundamental studies establish a microscopic-level description of ion-intercalation redox chemistry inside the nanoconfined pores of conductive MOF nanoparticles and porous materials for electrochemical intercalation chemistry in general.

## ASSOCIATED CONTENT

### Supporting Information

The Supporting Information is available free of charge at https://pubs.acs.org/doi/10.1021/jacs.2c12846.

> Additional synthetic experiments and details of $Fe(TA)_2$ nanoparticles; additional characterization data including SEM, DLS, XRD, XPS, FT-IR, and TGA of nanoparticle thin films; details and data for numerical simulations of anion intercalation reaction barriers (PDF)

## AUTHOR INFORMATION

### Corresponding Author

**Carl K. Brozek** − *Department of Chemistry and Biochemistry, Material Science Institute, University of Oregon, Eugene, Oregon 97403, United States;* orcid.org/0000-0002-8014-7904; Email: cbrozek@uoregon.edu

### Authors

**Jiawei Huang** − *Department of Chemistry and Biochemistry, Material Science Institute, University of Oregon, Eugene, Oregon 97403, United States*

**Checkers R. Marshall** − *Department of Chemistry and Biochemistry, Material Science Institute, University of Oregon, Eugene, Oregon 97403, United States*

**Kasinath Ojha** − *Department of Chemistry and Biochemistry, Material Science Institute, University of Oregon, Eugene, Oregon 97403, United States*

**Meikun Shen** − *Department of Chemistry and Biochemistry, Material Science Institute, University of Oregon, Eugene, Oregon 97403, United States;* orcid.org/0000-0001-8100-4115

**Stephen Golledge** − *Department of Chemistry and Biochemistry, Material Science Institute, University of Oregon, Eugene, Oregon 97403, United States*

**Kentaro Kadota** − *Department of Chemistry and Biochemistry, Material Science Institute, University of Oregon, Eugene, Oregon 97403, United States*

**Jacob McKenzie** − *Department of Chemistry and Biochemistry, Material Science Institute, University of Oregon, Eugene, Oregon 97403, United States*

**Kevin Fabrizio** − *Department of Chemistry and Biochemistry, Material Science Institute, University of Oregon, Eugene, Oregon 97403, United States;* orcid.org/0000-0001-9700-1824

**James B. Mitchell** − *Department of Chemistry and Biochemistry, Material Science Institute, University of Oregon, Eugene, Oregon 97403, United States*

**Faiqa Khaliq** − *Department of Chemistry and Biochemistry, Material Science Institute, University of Oregon, Eugene, Oregon 97403, United States*

**Audrey M. Davenport** − *Department of Chemistry and Biochemistry, Material Science Institute, University of Oregon, Eugene, Oregon 97403, United States*

**Michael A. LeRoy** − *Department of Chemistry and Biochemistry, Material Science Institute, University of Oregon, Eugene, Oregon 97403, United States*

**Ashley N. Mapile** − *Department of Chemistry and Biochemistry, Material Science Institute, University of Oregon, Eugene, Oregon 97403, United States*

**Tekalign T. Debela** − *Department of Chemistry and Biochemistry, Material Science Institute, University of Oregon, Eugene, Oregon 97403, United States;* orcid.org/0000-0003-4859-2597

**Liam P. Twight** − *Department of Chemistry and Biochemistry, Material Science Institute, University of Oregon, Eugene, Oregon 97403, United States*

**Christopher H. Hendon** − *Department of Chemistry and Biochemistry, Material Science Institute, University of Oregon, Eugene, Oregon 97403, United States;* orcid.org/0000-0002-7132-768X

Complete contact information is available at:
https://pubs.acs.org/10.1021/jacs.2c12846

## Notes

The authors declare no competing financial interest.

## ■ ACKNOWLEDGMENTS

This material is based upon work supported by the National Science Foundation through the Division of Materials Research under grant nos. DMR-2114430 and DMR-1956403. M.S. gratefully acknowledges funding from the Department of Energy, Basic Energy Sciences award no. DE-SC0014279. J.B.M. especially appreciates the support of US Office of Naval Research, grant N00014-20-1-2517 (to S.W.B.). C.K.B. and C.H.H. gratefully acknowledge support from the Research Corporation for Science Advancement (Cottrell Award). The authors are especially grateful to Shannon Boettcher and Paul Kempler for their invaluable discussions. They acknowledge the use of shared instrumentation in the Center for Advanced Materials Characterization in Oregon (CAMCOR) and the Phil and Penny Knight Campus for Accelerating Scientific Impact.

## ■ REFERENCES

(1) Feng, D.; Lei, T.; Lukatskaya, M. R.; et al. Robust and conductive two-dimensional metal-organic frameworks with exceptionally high volumetric and areal capacitance. *Nat. Energy* **2018**, *3*, 30−36.

(2) Hod, I.; Sampson, M. D.; Deria, P.; et al. Fe-Porphyrin-Based Metal-Organic Framework Films as High-Surface Concentration, Heterogeneous Catalysts for Electrochemical Reduction of $CO_2$. *ACS Catal.* **2015**, *5*, 6302−6309.

(3) He, B.; Zhang, Q.; Pan, Z.; et al. Freestanding Metal-Organic Frameworks and Their Derivatives: An Emerging Platform for Electrochemical Energy Storage and Conversion. *Chem. Rev.* **2022**, *122*, 10087−10125.

(4) Sheberla, D.; Bachman, J. C.; Elias, J. S.; et al. Conductive MOF electrodes for stable supercapacitors with high areal capacitance. *Nat. Mater.* **2017**, *16*, 220−224.

(5) Baumann, A. E.; Burns, D. A.; Liu, B.; Thoi, V. S. Metal-organic framework functionalization and design strategies for advanced electrochemical energy storage devices. *Commun. Chem.* **2019**, *2*, 1−14.

(6) Cai, G.; Yan, P.; Zhang, L.; Zhou, H. C.; Jiang, H. L. Metal-Organic Framework-Based Hierarchically Porous Materials: Synthesis and Applications. *Chem. Rev.* **2021**, *121*, 12278−12326.

(7) Chen, K.; Ray, D.; Ziebel, M. E.; Gaggioli, C. A.; Gagliardi, L.; Marinescu, S. C. Cu[Ni(2,3-pyrazinedithiolate)$_2$] Metal−Organic Framework for Electrocatalytic Hydrogen Evolution. *ACS Appl. Mater. Interfaces* **2021**, *13*, 34419−34427.

(8) Wang, Q.; Astruc, D. State of the Art and Prospects in Metal-Organic Framework (MOF)-Based and MOF-Derived Nanocatalysis. *Chem. Rev.* **2020**, *120*, 1438−1511.

(9) Xie, L. S.; Skorupskii, G.; Dincă, M. Electrically Conductive Metal-Organic Frameworks. *Chem. Rev.* **2020**, *120*, 8536−8580.

(10) Zhou, H. C.; Long, J. R.; Yaghi, O. M. Introduction to metal-organic frameworks. *Chem. Rev.* **2012**, *112*, 673−674.

(11) Furukawa, H.; Cordova, K. E.; O'Keeffe, M.; Yaghi, O. M. The chemistry and applications of metal-organic frameworks. *Science* **2013**, *341*, No. 1230444.

(12) Roy, S.; et al. Electrocatalytic Hydrogen Evolution from a Cobaloxime-Based Metal−Organic Framework Thin Film. *J. Am. Chem. Soc.* **2019**, *141*, 15942−15950.

(13) Johnson, B. A.; Beiler, A. M.; McCarthy, B. D.; Ott, S. Transport Phenomena: Challenges and Opportunities for Molecular Catalysis in Metal-Organic Frameworks. *J. Am. Chem. Soc.* **2020**, *142*, 11941−11956.

(14) Sharp, C. H.; Bukowski, B. C.; Li, H.; et al. Nanoconfinement and mass transport in metal-organic frameworks. *Chem. Soc. Rev.* **2021**, *50*, 11530−11558.

(15) Castner, A. T.; Su, H.; Grape, E. S.; et al. Microscopic Insights into Cation-Coupled Electron Hopping Transport in a Metal-Organic Framework. *J. Am. Chem. Soc.* **2022**, *144*, 5910−5920.

(16) Chmiola, J.; Yushin, G.; Gogotsi, Y.; et al. Anomalous Increase in Carbon Capacitance at Pore Sizes Less Than 1 Nanometer. *Science* **2006**, *313*, 1760−1763.

(17) Fleischmann, S.; Zhang, Y.; Wang, X.; et al. Continuous transition from double-layer to Faradaic charge storage in confined electrolytes. *Nat. Energy* **2022**, *7*, 222−228.

(18) Boyd, S.; Ganeshan, K.; Tsai, W. Y.; et al. Effects of interlayer confinement and hydration on capacitive charge storage in birnessite. *Nat. Mater.* **2021**, *20*, 1689−1694.

(19) Sood, A.; Poletayev, A. D.; Cogswell, D. A.; et al. Electrochemical ion insertion from the atomic to the device scale. *Nat. Rev. Mater.* **2021**, *6*, 847−867.

(20) Herm, Z. R.; Wiers, B. M.; Mason, J. A.; et al. Separation of Hexane Isomers in a Metal-Organic Framework with Triangular Channels. *Science* **2013**, *340*, 960−964.

(21) Yan, Z.; Li, M.; Gao, H. L.; Huang, X. C.; Li, D. High-spin versus spin-crossover versus low-spin: Geometry intervention in cooperativity in a 3D polymorphic iron(II)-tetrazole MOFs system. *Chem. Commun.* **2012**, *48*, 3960−3962.

(22) Cai, M.; Loague, Q.; Morris, A. J. Design Rules for Efficient Charge Transfer in Metal-Organic Framework Films: The Pore Size Effect. *J. Phys. Chem. Lett.* **2020**, *11*, 702−709.

(23) Marshall, C. R.; Timmel, E. E.; Staudhammer, S. A.; Brozek, C. K. Experimental evidence for a general model of modulated MOF nanoparticle growth. *Chem. Sci.* **2020**, *11*, 11539−11547.

(24) Wang, J.; Imaz, I.; Maspoch, D. Metal−Organic Frameworks: Why Make Them Small? *Small Struct.* **2022**, *3*, No. 2100126.

(25) Wang, S.; McGuirk, C. M.; d'Aquino, A.; Mason, J. A.; Mirkin, C. A. Metal−Organic Framework Nanoparticles. *Adv. Mater.* **2018**, *30*, No. 1800202.

(26) Romero-Angel, M.; Castells-Gil, J.; Rubio-Giménez, V.; et al. Surfactant-assisted synthesis of titanium nanoMOFs for thin film fabrication. *Chem. Commun.* **2021**, *57*, 9040−9043.

(27) Liu, Y.; Wang, J.; Imaz, I.; Maspoch, D. Assembly of Colloidal Clusters Driven by the Polyhedral Shape of Metal−Organic Framework Particles. *J. Am. Chem. Soc.* **2021**, *143*, 12943−12947.

(28) Barcus, K.; Lin, P.-A.; Zhou, Y.; Arya, G.; Cohen, S. M. Influence of Polymer Characteristics on the Self-Assembly of Polymer-Grafted Metal−Organic Framework Particles. *ACS Nano* **2022**, *16*, 18168−18177.

(29) Feng, G.; Huang, J.; Sumpter, B. G.; Meunier, V.; Qiao, R. Structure and dynamics of electrical double layers in organic electrolytes. *Phys. Chem. Chem. Phys.* **2010**, *12*, 5468−5479.

(30) Gándara, F.; et al. Porous, conductive metal-triazolates and their structural elucidation by the charge-flipping method. *Chem. - Eur. J.* **2012**, *18*, 10595−10601.

(31) Marshall, C. R.; Dvorak, J. P.; Twight, L. P.; et al. Size-Dependent Properties of Solution-Processable Conductive MOF Nanocrystals. *J. Am. Chem. Soc.* **2022**, *144*, 5784−5794.

(32) Park, J. G.; Aubrey, M. L.; Oktawiec, J.; et al. Charge Delocalization and Bulk Electronic Conductivity in the Mixed-Valence Metal-Organic Framework Fe(1,2,3-triazolate)$_2$(BF$_4$)$_x$. *J. Am. Chem. Soc.* **2018**, *140*, 8526−8534.

(33) Sánchez, M.; Sabio, L.; Gálvez, N.; Capdevila, M.; Dominguez-Vera, J. M. Iron chemistry at the service of life. *IUBMB Life* **2017**, *69*, 382−388.

(34) Cooper, S. R.; McArdle, Jv.; Raymond, K. N. Siderophore electrochemistry: relation to intracellular iron release mechanism. *Proc. Natl. Acad. Sci. U.S.A.* **1978**, *75*, 3551−3554.

(35) Saji, T.; Yamada, T.; Aoyagui, S. Electron-transfer rate constants for redox systems of Fe(III)/Fe(II) complexes with 2,2′-bipyridine and/or cyanide ion as measured by the galvanostatic double pulse method. *J. Electroanal. Chem.* **1975**, *61*, 147−153.

(36) Bondarenko, A. S.; Stephens, I. E. L.; Hansen, H. A.; et al. The Pt(111)/Electrolyte Interface under Oxygen Reduction Reaction Conditions: An Electrochemical Impedance Spectroscopy Study. *Langmuir* **2011**, *27*, 2058−2066.

(37) Wade, C. R.; Li, M.; Dincă, M. Facile Deposition of Multicolored Electrochromic Metal-Organic Framework Thin Films. *Angew. Chem., In. Ed.* **2013**, *52*, 13377−13381.

(38) Andreeva, A. B.; et al. Cooperativity and Metal−Linker Dynamics in Spin Crossover Framework Fe(1,2,3-triazolate)$_2$. *Chem. Mater.* **2021**, *33*, 8534−8545.

(39) Mitchell, J. B.; Wang, R.; Ko, J. S.; Long, J. W.; Augustyn, V. Critical Role of Structural Water for Enhanced Li$^+$ Insertion Kinetics in Crystalline Tungsten Oxides. *J. Electrochem. Soc.* **2022**, *169*, No. 030534.

(40) Tsai, W. Y.; Taberna, P. L.; Simon, P. Electrochemical quartz crystal microbalance (EQCM) study of ion dynamics in nanoporous carbons. *J. Am. Chem. Soc.* **2014**, *136*, 8722−8728.

(41) Levi, M. D.; Lukatskaya, M. R.; Sigalov, S.; et al. Solving the Capacitive Paradox of 2D MXene using Electrochemical Quartz-Crystal Admittance and In Situ Electronic Conductance Measurements. *Adv. Energy Mater.* **2015**, *5*, No. 1400815.

(42) Koper, M. T. M.; Lukkien, J. J. Modeling the butterfly: the voltammetry of $(\sqrt{3}\times\sqrt{3})$R30° and p(2×2) overlayers on (111) electrodes. *J. Electroanal. Chem.* **2000**, *485*, 161−165.

(43) Koper, M. T. M.; Lukkien, J. J. Modeling the butterfly: influence of lateral interactions and adsorption geometry on the voltammetry at (111) and (100) electrodes. *Surf. Sci.* **2002**, *498*, 105−115.

(44) Ojha, K.; Doblhoff-Dier, K.; Koper, M. T. M. Double-layer structure of the Pt(111)−aqueous electrolyte interface. *Proc. Natl. Acad. Sci. U.S.A.* **2022**, *119*, No. e2116016119.

(45) Cooper, S. J.; Bertei, A.; Finegan, D. P.; Brandon, N. P. Simulated impedance of diffusion in porous media. *Electrochim. Acta* **2017**, *251*, 681−689.

(46) O'Toole, T. R.; Younathan, J. N.; Sullivan, B. P.; Meyer, T. J. 1,2-Difluorobenzene: a relatively inert and noncoordinating solvent for electrochemical studies on transition-metal complexes. *Inorg. Chem.* **1989**, *28*, 3923−3926.

(47) Wang, H.; Kim, S. C.; Rojas, T.; et al. Correlating Li-Ion Solvation Structures and Electrode Potential Temperature Coefficients. *J. Am. Chem. Soc.* **2021**, *143*, 2264−2271.

(48) Andreeva, A. B.; Le, K. N.; Chen, L.; et al. Soft Mode Metal-Linker Dynamics in Carboxylate MOFs Evidenced by Variable-Temperature Infrared Spectroscopy. *J. Am. Chem. Soc.* **2020**, *142*, 19291−19299.

(49) Schmid, M. J.; Bickel, K. R.; Novák, P.; Schuster, R. Microcalorimetric measurements of the solvent contribution to the entropy changes upon electrochemical lithium bulk deposition. *Angew. Chem., Int. Ed.* **2013**, *52*, 13233−13237.

(50) Xu, Z. L.; Yoon, G.; Park, K. Y.; et al. Tailoring sodium intercalation in graphite for high energy and power sodium ion batteries. *Nat. Commun.* **2019**, *10*, No. 2598.

(51) Kung, C. W.; et al. Increased electrical conductivity in a mesoporous metal−organic framework featuring metallacarboranes guests. *J. Am. Chem. Soc.* **2018**, *140*, 3871−3875.

(52) Brus, J.; Czernek, J.; Urbanova, M.; Rohlicek, J.; Plecháček, T. Transferring Lithium Ions in the Nanochannels of Flexible Metal−Organic Frameworks Featuring Superchaotropic Metallacarborane Guests: Mechanism of Ionic Conductivity at Atomic Resolution. *ACS Appl. Mater. Interfaces* **2020**, *12*, 47447−47456.